Low-wavenumber turbulent boundary layer wall-pressure measurements from vibration data on a cylinder in pipe flow

William K. Bonness *, Dean E. Capone, Stephen A. Hambric

Applied Research Laboratory, The Pennsylvania State University, PO Box 30, State College, PA 16804-0030, USA

A R T I C L E   I N F O

A B S T R A C T

The response of a structure to turbulent boundary layer (TBL) excitation has been an area of research for roughly 50 years, although uncertainties persist surrounding the low-wavenumber levels of the TBL surface pressure spectrum. In this experimental investigation, a cylindrical shell with a smooth internal surface is subjected to TBL excitation from water in fully developed pipe flow. The cylinder's vibration response to this excitation is used to determine low-wavenumber TBL surface pressure levels at lower streamwise wavenumbers than previously reported ($k_1/k_c < 0.01$). An experimental modal analysis is also conducted on the water-filled cylindrical shell to determine structural parameters which are used to extract TBL pressures. The measured low-wavenumber pressure data falls midway between TBL models by Smol'yakov [*Acoustical Physics* 52(3) (2006) 331–337] and Chase [*Journal of Sound and Vibration* 112(1) (1987) 125–147] and is roughly 23 dB lower than an early TBL model by Corcos [*Journal of the Acoustical Society of America* 35(2) (1963) 192–198]. The current data is a few decibels below the lower bound of related measurements in air by Farabee and Geib [*ICIASF '75 Record*, 1975, pp. 311–319] and Martin and Leehey [*Journal of Sound and Vibration* 52(1) (1977) 95–120]. A simple wavenumber white form for the TBL surface pressure spectrum at low-wavenumber is suggested.

© 2010 Elsevier Ltd. All rights reserved.

1. Introduction

As a boundary layer develops and grows in the fluid near the surface of a moving vehicle (or in flow over a stationary body), turbulent eddies of varying scales are generated due to the shearing of the fluid layers within the boundary layer. These eddies decay and regenerate over a relatively short distance, are correlated over a limited region, and cause velocity fluctuations throughout the boundary layer. The integrated effect of these velocity fluctuations produces fluctuating pressures on the surface of the underlying structure as depicted in Fig. 1.

Fluctuating pressures, correlated over some surface area, generate fluctuating forces that can radiate sound directly and can also excite the underlying structure producing undesirable vibration and radiated sound. Past research has demonstrated the significance of this phenomenon in generating interior aircraft cabin noise and in understanding and mitigating the vibration and acoustic radiation of marine vehicles [1–3].

Most of the energy in a turbulent boundary layer is contained at wavenumbers associated with eddy convection, $k_c = \omega/U_c$, where k_c is the convective wavenumber, ω is the radian frequency, and U_c is the convection velocity which is related to the average speed at which eddies travel. Fig. 2 shows a schematic of the TBL streamwise wavenumber spectrum

---

* Corresponding author.
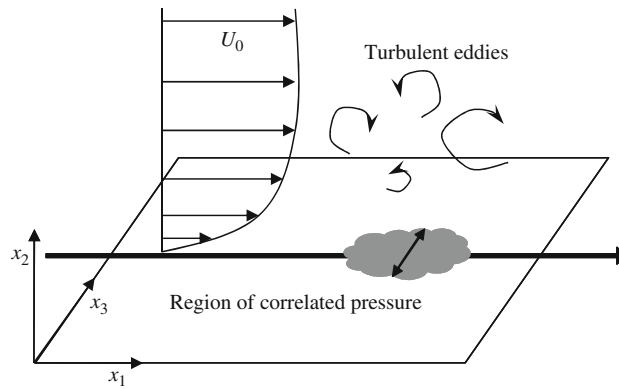   *E-mail address:* wkb3@only.arl.psu.edu (W.K. Bonness).

Fig. 1. Schematic of wall pressures from boundary layer turbulence over a surface.
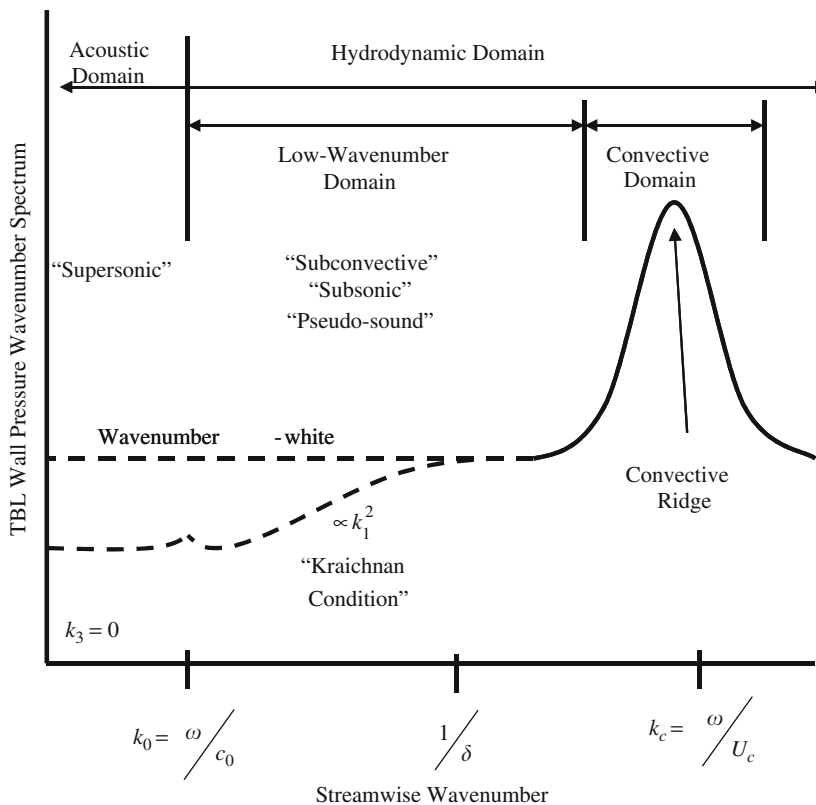

Fig. 2. Schematic of TBL wall pressure wavenumber spectrum on a log–log plot.

and the strong peak at the convective wavenumber. For the relatively high Mach number flow associated with aircraft cabin noise, convective wavenumbers in the flow tend to match wavenumbers of the bending waves in the underlying structures (aerodynamic coincidence). Therefore, cabin noise in commercial aircraft is predominantly caused by TBL excitation of the fuselage at convective wavenumbers.

However, for the low Mach number flow associated with marine applications, convective wavenumbers are too high to match those of the bending waves in the underlying structure and therefore do not cause significant vibration. The structural wavelengths of interest lie in the low-wavenumber portion of the surface pressure spectrum (defined as the region above the acoustic wavenumber, $k_0 = \omega/C_0$, and below the convective wavenumber, $k_c = \omega/U_c$). Although the low-wavenumber wall pressure levels beneath an attached, neutral pressure gradient, TBL are roughly 1/100th of the convective wavenumber levels (40 dB below), these low-wavenumber pressures are responsible for structural vibration and sound. However, because the levels are so low relative to the convective wavenumber pressures, they have historically

been very difficult to measure and model correctly. A review of the extensive literature in the area of TBL wall pressures reveals a general lack of measured wall pressures at especially low wavenumbers ($k_1/k_c < 0.01$).

Most measurements of low-wavenumber TBL wall pressure have been made in air at relatively high Mach numbers over smooth surfaces. However, making these measurements in water has some distinct advantages since measurements can be made at lower Mach number extending the low-wavenumber region of the wall pressure spectrum. The higher speed of sound in water shifts the acoustic wavenumber downward and the lower practical speeds of vehicles (and measurement facilities) shifts the convective wavenumber upward. This broadens the low-wavenumber range at both ends. Also, the higher density of water generates higher surface pressures (even at low speeds), which increases the signal-to-noise ratio.

In this work, an experimental facility and measurement approach is developed and presented for measuring low-wavenumber TBL fluctuating pressures in water over a smooth surface. By measuring the vibration of a structure subjected to TBL excitation, one can inversely determine the low-wavenumber pressure required to generate the structural response. This was first done by Martin and Leehey [4] using a flexible membrane in air. In the present case, a thin cylindrical shell is subjected to excitation from fully developed pipe flow in water, and wall pressures are presented at lower streamwise wavenumbers than previously reported ($k_1/k_c < 0.01$).

2. TBL wall pressure models and measured data

2.1. TBL wall pressure models

On the surface of a structure beneath a locally homogeneous turbulent boundary layer, the correlation between fluctuating pressure, p, at a point, x_1, x_3, and time, t, and a second point separated from p in space and time by ξ_1, ξ_3 and τ, respectively, can be represented with a statistical space–time correlation function [2]

$$R(\xi_1,\xi_3,\tau) = \langle p(x_1,x_3,t)p(x_1+\xi_1,x_3+\xi_3,t+\tau)\rangle, \tag{1}$$

where the brackets, $\langle \ \rangle$, represent an ensemble average. The cross-spectrum is found by taking its temporal Fourier Transform

$$\Gamma(\xi_1,\xi_3,\omega) = \frac{1}{2\pi}\int_{-\infty}^{\infty} R(\xi_1,\xi_3,\tau)e^{-i\omega\tau}\,d\tau, \tag{2}$$

and the wavevector–frequency spectrum is found by taking both the spatial and temporal Fourier Transforms

$$P(k_1,k_3,\omega) = \frac{1}{(2\pi)^3}\int_{-\infty}^{\infty}\int_{-\infty}^{\infty}\int_{-\infty}^{\infty} R(\xi_1,\xi_3,\tau)e^{-i(k_1\xi_1+k_3\xi_3+\omega\tau)}\,d\xi_1\,d\xi_3\,d\tau, \tag{3}$$

The streamwise variables in Eqs. (1) through (3) are x_1, ξ_1, k_1 and the cross-flow variables are x_3, ξ_3, k_3.

Corcos [5] used two-point cross-correlation measurements of wall pressure by Willmarth and Wooldridge [6] and by Bakewell et al. [7] in fully developed pipe flow, as the basis for an early form of a TBL surface pressure model. He proposed a separable form for the cross-spectrum of pressure on the surface below spatially homogenous boundary layer turbulence. The separable function includes factors for the surface pressure point frequency spectrum, $\phi(\omega)$, exponentially decaying terms involving the non-dimensional streamwise and cross-flow separation distances and an oscillating or propagating function of non-dimensional separation distance in the flow direction. The point frequency spectrum of wall pressure is related to the wavevector–frequency spectrum by $\phi(\omega) = \int_{-\infty}^{\infty}\int_{-\infty}^{\infty} P(k_1,k_3,\omega)\,dk_1\,dk_3$.

The spatial and temporal separability of the Corcos cross-spectrum enable the frequency spectrum and wavenumber spectrum to be evaluated independently. The wavevector spectrum is notably flat very near zero wavenumber. While this model has shown remarkable utility, it is widely accepted that the low-wavenumber levels overestimate actual TBL surface pressure levels. Modifications to the original Corcos model have been proposed by others [8,9] attempting to better match the low-wavenumber levels to available data.

Chase [10] proposed another popular TBL surface pressure model based on the relationship between the velocity field and fluctuating pressures from the Poisson equation. Chase intended to model the entire hydrodynamic domain and address the low-wavenumber limitations of the Corcos model. Chase cast his model directly in the wavenumber domain, consequently there is no simple inverse Fourier transformation to get a cross-spectral density function. Also in contrast to the Corcos model, the Chase model is non-separable in frequency and wavevector.

Chase did however propose a nearly separable form of his wavevector–frequency spectrum, which can be integrated over wavenumber to provide an exact form for the two-sided wall pressure frequency spectrum

$$\frac{\phi(\omega)}{\rho^2 U_0^3 \delta} = \left(\frac{u_\tau}{U_0}\right)^4 \frac{\left((\omega\delta/U_0)^2 + \alpha_1^2\right)}{\left((\omega\delta/U_0)^2 + 1\right)^{1.5}}, \tag{4}$$

where δ is the pipe radius, U_0 the pipe centerline velocity, u_τ the friction velocity, and $\alpha_1 \approx 0.2$ is an empirical constant which controls the low frequency level and slope. Use of this model for unbounded flows requires substituting boundary layer thickness for pipe radius and freestream velocity for pipe centerline velocity.

In general, the point wall pressure frequency spectrum, $\phi(\omega)$ can be characterized by four frequency regions: (1) the low frequency region where levels increase as roughly ω^2, (2) the spectral peak region, (3) the inertial subrange, universal range, or scale independent range where levels are roughly $\phi(\omega) \approx \rho^2 u_t^4 \omega^{-1}$, and (4) the high frequency or viscous subrange which exhibits a roughly exponential roll-off from the universal range. The Chase spectrum of Eq. (4) does not contain the viscous subrange so its use is limited to relatively high Reynolds number and low reduced frequencies. However, the Chase point frequency spectrum can be multiplied by an exponential decay factor, $e^{-2.2(\omega v/u_\tau)}$ to account for the viscous subrange of measured data at high frequencies. This factor comes from a curve fit by Lysak based on results from modeling the turbulent velocity spectrum [11].

Guided by theoretical arguments of Kraichnan [12], the original Chase wavevector–frequency model goes to zero very near zero wavenumber in contrast to the Corcos model which remains essentially constant near zero wavenumber. Chase offered improvements to the original model [10] with the addition of terms accounting for the acoustic domain [13] and rotational or viscous contributions [14]. While the Chase model addresses some of the low-wavenumber limitations of the Corcos model, it lacks experimental validation in the acoustic domain and the lowest hydrodynamic wavenumbers.

A recent comprehensive wavevector–frequency model (and cross-spectral density function) of TBL surface pressure is reported by Smol'yakov [15]. This model is a generalization and extension of an earlier model proposed by Smol'yakov and Tkachenko [16]. The revised model includes a dependence on Reynolds number and accounts for the effects of viscosity not included in the original 1991 model. Like the Corcos model, the Smol'yakov [15] model contains separable functions of time and spatial separation distance and can be easily transformed between the cross-spectrum and the wavevector–frequency spectrum. The wall pressure frequency autospectrum accompanying this model was proposed by Smol'yakov [17].

Graham [3] reports and compares other TBL surface pressure models including those of Ffowcs Williams [8] and Efimtsov [18]. Common to all these models is the peak in the wavenumber spectrum at the convective wavenumber. Essentially all TBL pressure models contain similar character in the convective peak vicinity. However, the discrepancy in the low-wavenumber region, below the convective peak, is the source of some controversy. Theoretical arguments for incompressible flow suggest a squared dependence on streamwise wavenumber [12], however the limited available data suggests a wavenumber "white" or flat streamwise wavenumber dependence.

2.2. Measurements of low-wavenumber data

Mapping out the entire TBL wavevector–frequency surface pressure spectrum experimentally has been difficult because of the difficulty in accurately measuring low-wavenumber pressures. The shape of the wavenumber spectrum near the convective peak has been relatively well established from two-point, cross-spectral density measurements between flush mounted pressure transducers [2]. However, at large transducer separation distances, needed to resolve the low-wavenumber spectrum, these measurements are typically overwhelmed by convective pressures and cannot be reliably used. Several wavenumber filtering schemes have been implemented to filter out the convective TBL and background acoustic pressures and to isolate low-wavenumber TBL pressures. Nearly all of this work has involved flow over smooth surfaces.

One class of low-wavenumber measurements involves using surface pressure transducers to measure wall pressure directly. Maidanik [19] proposed a wavenumber filtering scheme in which a streamwise array of flush mounted pressure sensors with appropriate sensor size and separation distance are summed with alternate phasing to determine pressure levels at discrete wavenumbers and frequencies. This method was implemented by Blake and Chase [20] and Farabee and Geib [21] in air using four and six sensor arrays, respectively. The method is fairly effective at filtering out background noise present in the acoustic domain, but is less effective at filtering out convective pressures. More recent direct measurements of pressure were conducted by Manoha [22] and Abraham and Keith [23] in water using large sensors arrays of 32 and 48 sensors, respectively. A spatial Discrete Fourier Transform was applied to the measured data to extract the entire streamwise wavenumber spectrum. Aliasing and leakage effects limited the low-wavenumber filtering to roughly 30 dB below the convective peak.

The second class of filtering methods involves measuring the vibration response of a structure subjected to TBL excitation to indirectly determine the low-wavenumber level of TBL pressure. This indirect measurement scheme is often termed an "inverse method" and utilizes the filtering effects of a flexible structure to isolate low-wavenumber pressures. This method more successfully filters out convective wavenumbers, but can be somewhat less successful at rejecting background noise contaminating the acoustic wavenumber domain. Data measured by Martin and Leehey [4] using a membrane in air is frequently cited as reliable low-wavenumber data [10,15].

Representative low-wavenumber data from Martin and Leehey [5] and Farabee and Geib [21] are plotted against curves generated using the models of Corcos [5], Chase [13], and Smol'yakov [15] in non-dimensional form in Fig. 3. Positive streamwise wavenumbers are plotted on a logarithmic scale with $k_3=0$. This figure illustrates the differences between existing TBL wavenumber models and past data measured in air. Also shown in this figure is the wavenumber range of expected data using the present indirect measurement approach of a cylinder in water.
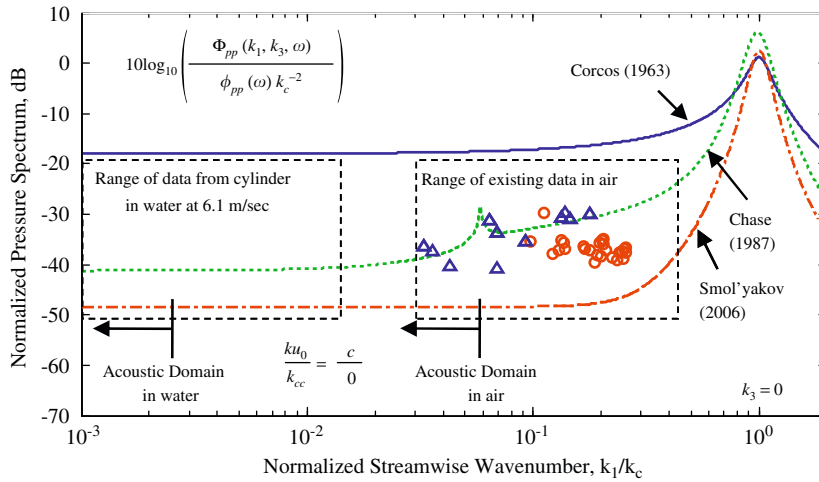
Fig. 3. Comparison of historical low-wavenumber TBL surface pressure data from measurements in air with TBL surface pressure models at conditions representative of data: ○ Martin and Leehey data [1]; △ Farabee and Geib data [18].

2.3. The inverse method for measuring low-wavenumber TBL pressure

The inverse method for measuring low-wavenumber TBL pressure focuses on measuring the peak resonance response of individual structural modes to TBL excitation. This requires information about the structure's dynamic response. For a given structure, the transfer function, or the Frequency Response Function (FRF), between the displacement u at a point α and the force F at a point β for an individual mode, n, is given by Ewins [24]

$$\frac{u_n(\alpha,\omega)}{F(\beta,\omega)} = \frac{1}{m_n}\frac{\psi_n(\alpha)\psi_n(\beta)}{[-\omega^2+\omega_n^2+\mathrm{i}\eta_n\omega_n\omega]}. \tag{5}$$

The four modal parameters of each structural mode in Eq. (5) are: angular resonance frequency, ω_n, loss factor, η_n, normalized structural normal mode shape function with a peak value of one, ψ_n, and the modal mass, m_n. The modal force F_n can be related to the force at point β by $F_n(\omega)=\psi_n(\beta)F(\beta, \omega)$. Therefore, displacement at a point on the structure is related to the modal force for a given mode by

$$u_n(\alpha,\omega) = \frac{1}{m_n}\frac{\psi_n(\alpha)F_n(\omega)}{[-\omega^2+\omega_n^2+\mathrm{i}\eta_n\omega_n\omega]}. \tag{6}$$

The modal force can in turn be related to the TBL wavevector–frequency spectrum [25] by

$$|F_n(\omega)|^2 = \int_{-\infty}^{+\infty}\!\!\int |S_n(k_1,k_3)|^2 P(k_1,k_3,\omega)\,\mathrm{d}k_1\,\mathrm{d}k_3. \tag{7}$$

where $s_{mn}(k_1, k_3)$ is the sensitivity or filter shape function—a spatial Fourier transform of $\psi_n(x_1, x_3)$

$$S_n(k_1,k_3) = \iint_A \psi_n(x_1,x_3)\mathrm{e}^{\mathrm{i}k_1x_1}\mathrm{e}^{\mathrm{i}k_3x_3}\,\mathrm{d}x_1\,\mathrm{d}x_3. \tag{8}$$

The proposed current measurement scheme for inversely determining low-wavenumber TBL surface pressures involves measuring the vibration response of a section of pipe (or a clamped cylindrical shell) to TBL pipe flow excitation in water and measuring the modal parameters of a water-filled cylindrical shell. A summary of the steps is outlined below:

1. The vibration response of a water-filled cylindrical shell subjected to TBL excitation at fully developed pipe flow conditions (6.1 m/s) is measured using a ring array of accelerometers.
2. Resonance frequency and damping for identified modes are extracted from the measured data in step 1.
3. A standard experimental modal analysis is conducted on the cylindrical shell filled with water to determine the spatial mode shapes and modal mass for each mode identified in step 2.
4. The normalized mode shapes of the cylinder are transformed to the wavenumber domain to determine the sensitivity functions from Eq. (8).
5. To start the iterative solution, a constant low-wavenumber pressure spectrum level at and around the modal wavenumber is assumed and the modal force for each mode is computed through numerical integration using Eq. (7).
6. The frequency response function for a single mode is combined with the modal force using Eq. (6) and expected TBL induced cylinder vibration levels are computed.

7. The expected vibration levels (step 6) are compared with the measured vibration levels (step 1) to evaluate assumed pressure spectrum levels.
8. Assumed low-wavenumber TBL pressure levels are adjusted until they produce the measured vibration.

3. TBL measurements using a cylindrical shell

3.1. Experimental evaluation of cylindrical shell response to fully developed pipe flow

The present work utilizes the Garfield Thomas Water Tunnel at the Applied Research Lab/Penn State University [26], shown in Fig. 4, as a 400 kl reservoir of water and capitalizes on the available hydrostatic head when the tunnel is filled. A long straight run of 150 mm diameter schedule 40, PVC pipe is connected to the lower leg of the tunnel and the pressure head above the pipe drives flow through a test-section (within the continuous pipe) into a reserve tank below the floor. The thin-walled aluminum cylindrical shell test-section is installed near the end of the straight pipe run which provides roughly 90 pipe diameters downstream from a flow conditioning device to the test-section. Flow conditioning is accomplished using a perforated plate or flow straightening device [27] installed just downstream of a large radius 90° elbow. The major advantage of this facility over more traditional flow facilities is that no moving parts or machines are involved in driving the flow which minimizes the background noise and vibration problem.

Available static pressure head from the filled water tunnel can generate a flow speed of 6.1 m/s in the 150 mm diameter pipe. The velocity change measured by a pitot-static probe in the pipe centerline as the water level drops during the 41 s time window required for data acquisition is $\pm 1\%$ from the average velocity. This system is very nearly steady-state over the data acquisition time period.

The cylindrical shell test-section, shown in Fig. 5, is machined from a 1.22 m long, 150 mm diameter, schedule 40 (7.1 mm thick) aluminum pipe. A 0.61 m long mid-section of pipe is machined from the outside down to a wall thickness of 3.2 mm to create the actual thin-walled test-section. The pipe inside surface is also machined to create a constant inside diameter (measured at 156 mm), a constant test-section wall thickness, and a smooth interior surface. Circumferential V-shaped grooves are machined around the pipe at the discontinuity between the uncut pipe and the ends of the test-section to a depth of 0.64 mm. The grooves are used to help simulate simply supported conditions at the test-section boundaries. Large aluminum blocks are rigidly bolted around the uncut portion of pipe adjacent to the grooves and rigidly attached to the floor which resides 23 cm below the pipe centerline. The rigid blocks, grooves, corner braces, and sand bags, shown in Fig. 5, help limit motion of the test-section end boundaries and help limit vibrational energy from crossing those boundaries.

Only flow over the 0.61 m long test-section is intended to impart energy to the thin cylinder walls. The structural discontinuities marking the edges of the test-section are only on the outside of the pipe and create an abrupt change in pipe wall thickness which acts as an impedance discontinuity. The internal flow does not experience any surface discontinuities at the leading or trailing edges of the test-section. The 1.22 m long aluminum pipe (in which the 0.61 m long test-section resides) is flanged and bolted between two sections of schedule 40, PVC pipe. Care was taken to minimize the gap between the pipe sections at the flanges.
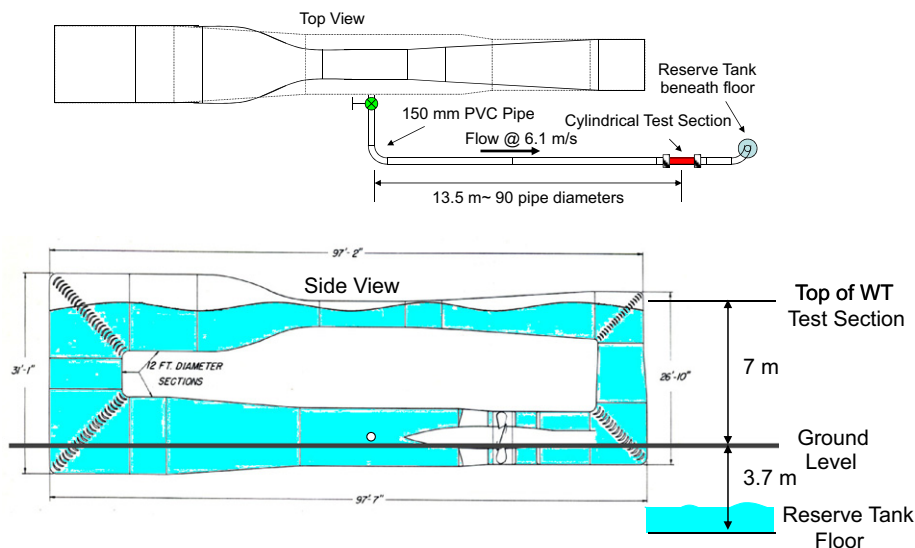

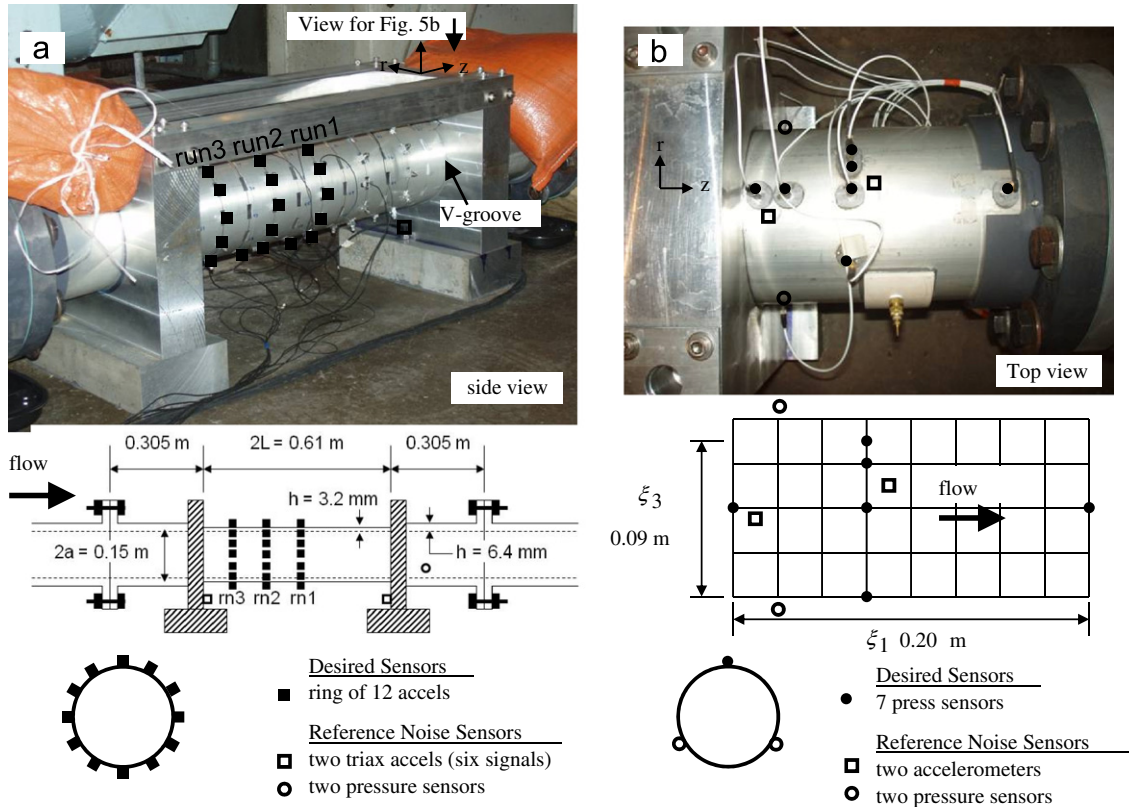**Fig. 4.** Experimental facility (ARL Water Tunnel), piping, and cylindrical test-section.

Fig. 5. Experimental test-section and flow measurement scheme: (a) accelerometer array and reference noise sensors and (b) pressure sensor array and reference noise sensors.

Two line arrays of flush mounted wall pressure sensors are installed downstream of the test-section in the uncut portion of the 1.22 m long aluminum pipe shown in Fig. 5. One array is aligned with the flow while the second is perpendicular to the flow. A ring array of 12 accelerometers is attached around the shell using Loctite adhesive at a single axial location corresponding to an evenly spaced grid. Three runs are conducted at the same flow conditions to allow moving the ring array of accelerometers to three different axial locations ($x/L = 1/2$, 1/3, 1/6) shown in Fig. 5. The variable mass loading effect of moving accelerometers to different measurement locations is minimized by placing dummy masses (representing an accelerometer) at all grid locations unoccupied by an accelerometer.

In addition to the accelerometer and dynamic pressure sensor arrays, a pitot-static probe is installed in the pipe centerline 1.5 m downstream from the test-section, and two wall mounted static pressure taps are installed 0.91 m apart spanning the 0.61 m long test-section. The pressure difference across the pitot-static probe and the static pressure drop across the test-section are measured using differential pressure transducers. The pitot probe and wall pressure taps provide measurements of the pipe centerline velocity and wall shear stress, respectively. The time domain accelerometer signals, dynamic pressure signals, and differential static pressure signals are all acquired simultaneously using an Agilent multi-channel data acquisition system sampling at 26,500 Hz.

3.2. Data post-processing

A noise removal technique is successfully implemented to remove remaining unwanted noise from measured TBL induced signals. The unwanted noise includes background acoustic pressures and test-section vibration not associated with TBL induced vibration. In addition to the sensors installed to measure TBL induced vibration and pressure (TBL sensors), additional dynamic pressure sensors and accelerometers are installed at various locations to act as reference sensors for measuring noise (noise sensors) as shown in Fig. 5. Two reference pressure sensors are installed in the same axial plane as the second most upstream TBL sensor (120° apart) to form a three-sensor array. The separation distances between the reference pressure sensors and the TBL pressure sensors allow uncorrelated TBL pressures to be determined for all frequencies of interest [28]. In addition, two reference accelerometers are placed near the TBL pressure sensors to

measure local pipe vibrations. Two additional tri-axial accelerometers are placed on the test-section supports to measure the test-section boundary vibrations at both ends in all three coordinate directions.

Because the unwanted noise produces correlated signals over long distances and the TBL induced signals do not, any portion of a TBL sensor signal coherent with a noise sensor signal can be removed leaving only the TBL induced signals. This technique is outlined using conditioned spectral densities by Bendat and Persol [29].

3.3. Experimental modal analysis

To determine actual mode shapes and modal masses associated with the resonance peaks identified in the flow data, a modal analysis is conducted on the test-section in the radial direction with the cylinder and adjacent piping full of water. To acquire the modal transfer function data needed for the modal analysis, an evenly spaced 156 point grid (13 points axially by 12 points circumferentially) is excited with a roving force hammer in reciprocal manner. Frequency Response Functions (FRFs) are simultaneously measured between the force hammer and four reference accelerometers representing drive point locations at various axial and circumferential locations on the grid.

After acquiring the FRF data, it is post-processed using standard modal analysis techniques to extract resonance frequency, damping, modal mass, and mode shape for identifiable cylinder resonances and modes. The Complex Mode Indicator Function (CMIF) technique is initially used to separate modes and identify resonance frequencies and mode shapes [30]. A Rational Fraction Polynomial scheme [24] is then used to refine the resonance frequency and damping estimates. Finally, a surface average of measured FRF data is compared to corresponding FRF estimates using Eq. (5) to determine the modal masses.

4. Results of experimental investigation

4.1. Flow measurement results

From measurements of total and static pressure using the pitot-static probe installed at the pipe centerline, pipe centerline flow velocity can be computed. For the three flow runs described earlier, centerline velocities range from 6.5 to 6.8 m/s. All dynamic wall pressure spectra and cylinder vibration spectra presented in this work are scaled to represent a common reference flow velocity of 6.1 m/s.

Convection velocity is computed from the phase between pairs of dynamic pressure sensors in the streamwise direction. Results from the measured data agree with an estimate for convection velocity suggested by Ko [31] based on work by Bull [32] where

$$\frac{U_c}{U_0} \cong 0.6 + 0.4 e^{-0.8\omega\delta^*/U_0}. \tag{9}$$

Above 200 Hz, the Ko approximation reasonably represents the measured data so it is used throughout this work to represent convection velocity for all subsequent analyses. Boundary layer displacement thickness, based on $\delta^* = 1/8\delta$ [33] where δ is the pipe radius, is 9.8 mm. Static pressure drop measurements indicate a friction factor, $f = 0.011$ (hydraulically smooth) and a friction velocity of $u_\tau/U_0 = 0.032$.

Measured frequency autospectra from the seven pressure sensors are averaged together for the three flow runs and shown in Fig. 6. Both the as-measured and reduced-noise spectra are shown. The peaks removed from the measured spectra below 100 Hz are likely acoustic pressures as they are removed due to coherence with pressure sensors mounted on the opposite pipe wall. Smaller peaks in the measured pressures above 100 Hz are likely induced by local pipe vibration as they are removed due to coherence with accelerometers installed adjacent to the pressure sensors.

The reduced-noise pressure spectra are also compared with two theoretical curves in Fig. 6. One is the Chase model of TBL frequency spectra (Eq. (4) with the high frequency exponential decay factor based on Lysak [11]) plotted for these conditions, and the second represents the actual signal a sensor of the size used for these measurements is expected to measure. The high frequency attenuation visible in the measured data and reflected in the second curve is due to the well known effect of area averaging over the sensor [5]. This attenuation is a measurement artifact and does not reflect the actual pressure on the surface of the structure. To determine the expected area averaged curve, the Chase TBL wavevector pressure spectrum is multiplied by a sensor response function and integrated over all wavenumbers. The integrated Chase curve shows good agreement with the measured data, therefore the Chase frequency spectrum represents the true wall pressure spectrum. The Chase true point spectrum (with exponential factor included) is used to represent the measured point frequency spectrum in subsequent analyses.

Measured cylinder vibration spectra in response to TBL excitation for the three different accelerometer ring locations are averaged together and shown in Fig. 7. Both the as-measured and reduced-noise spectra are shown. The energy removed from the as-measured spectra are removed due to coherence with accelerometers attached to the test-section supports. This represents energy in the surrounding facility which interferes with the TBL induced pipe wall vibrations. The amount of energy removed from various resonance peaks depends in part on the structural mode. The reduced-noise vibration levels are decomposed into circumferential Fourier components which reveal low-order cylinder modes from
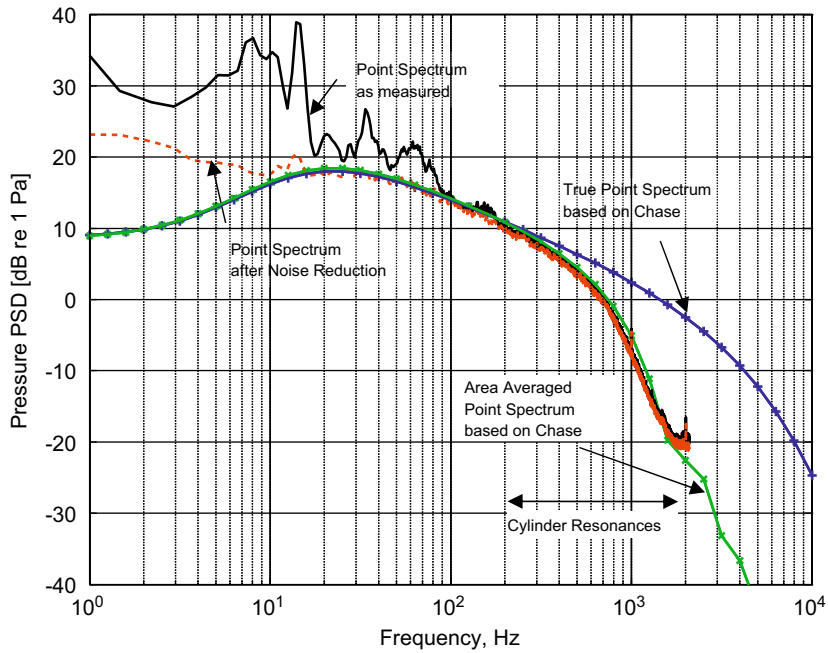
Fig. 6. Comparison of measured TBL point frequency spectrum with Chase model accounting for sensor area averaging.
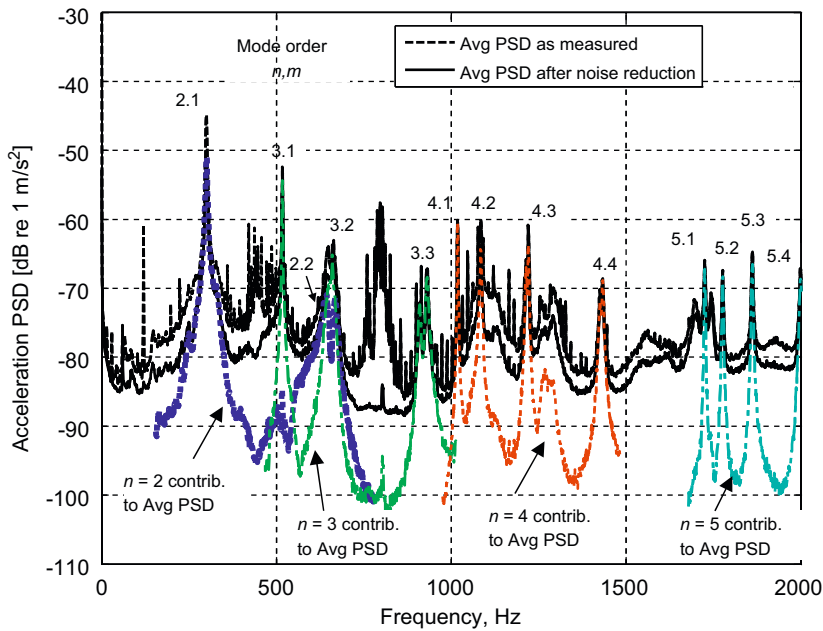

Fig. 7. Cylindrical shell average measured vibration with flow at 6.1 m/s decomposed into circumferential Fourier components.

n=2 to 5 below 2000 Hz. These resonance peaks represent the TBL induced cylinder vibration levels from which the low-wavenumber TBL pressures can be determined.

4.2. Modal parameter estimation

To estimate TBL induced cylinder vibration from modal forces using Eq. (6), four modal parameters are needed to compute vibration estimates for each mode. For modes identified in the measured flow data, resonance frequency and damping are obtained from the flow data based on the resonance peak frequency and the half-power points, respectively.

Table 1
Cylindrical shell experimental modal parameters.

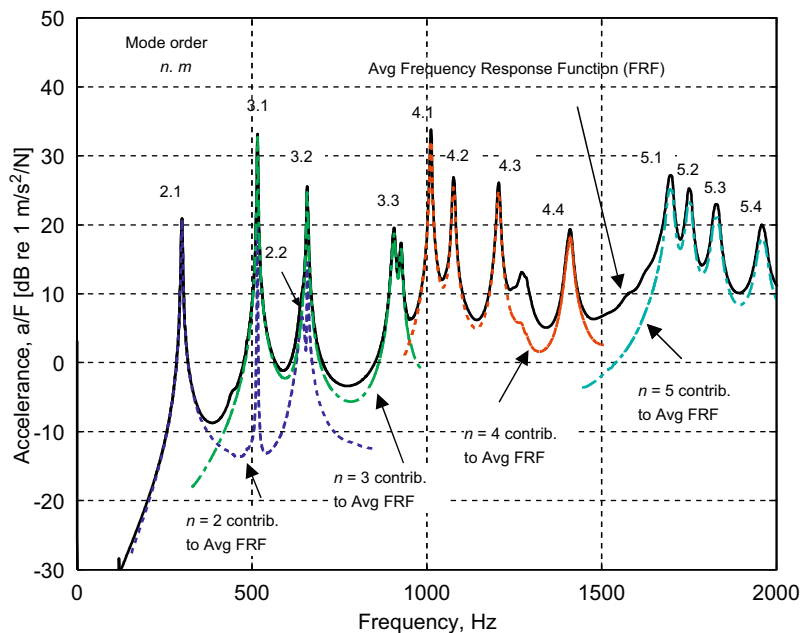| Mode n,m	Res. freq. (Hz)	Damping (%)	Modal mass (kg)	Low wavenumber pressure level (see Fig. 11)
2,1	301	0.007	3.8	−38
3,1	517.5	0.003	3.0	−41
2,2	643	0.02	3.2	−39
3,2	660	0.009	2.5	−40
3,3	910	0.009	2.4	−42
3,3	932	0.006	2.9	−41
4,1	1018	0.002	1.7	−43
4,2	1084	0.003	1.7	−42
4,3	1221	0.003	1.5	−41
4,4	1434	0.004	1.5	−43
5,1	1726	0.002	2.8	−37
5,2	1777	0.002	2.8	−40
5,3	1862	0.002	1.9	−40
5,4	1999	0.002	1.7	−42

Fig. 8. Cylindrical shell average Frequency Response Functions from modal analysis data decomposed into circumferential Fourier components.

Mode shape and modal mass are obtained from the experimental modal analysis. Table 1 includes values for the modal parameters extracted from the flow data and modal analysis for identified modes with relatively low damping.

For a perfectly axi-symmetric, homogenous, isotropic, thin-walled cylinder, all $n > 0$ modes occur as orthogonal pairs with identical resonance frequencies. Imperfections or slight asymmetry in an actual experimental cylinder tends to make the resonance frequencies for the orthogonal pairs closely spaced in frequency but not identical. Identifying both orthogonal modes in the modal analysis data was generally straight forward using available modal analysis techniques. However, identifying both modes of each orthogonal pair in the measured flow data was not always possible. To simplify the analysis, only one mode from each orthogonal pair was selected to represent each mode order. In cases where it was not obvious which of the two modes identified in the modal analysis corresponded with a resonance peak in the flow data, modal parameters from the mode with the lowest damping were attributed to the flow resonance peak.

A plot of the surface averaged acceleration from the modal analysis measurements, decomposed into circumferential Fourier components, is shown in Fig. 8. The modal analysis data shows essentially the same spectral content as the measured cylinder vibration due to flow excitation shown in Fig. 7.

The cylindrical shell response functions or mode shapes determined from the modal analysis involve displacements in the radial direction. These mode shape functions, $\psi_{nm}(\phi, z)$, are characterized by a sinusoidal dependence where n represents the number of full wavelengths in the circumferential direction, and m represents the number of half-wavelengths in the axial direction. For the lowest order $n=0$ and 1 modes, only the $n=1$, $m=1$ mode (1,1) is visible in the
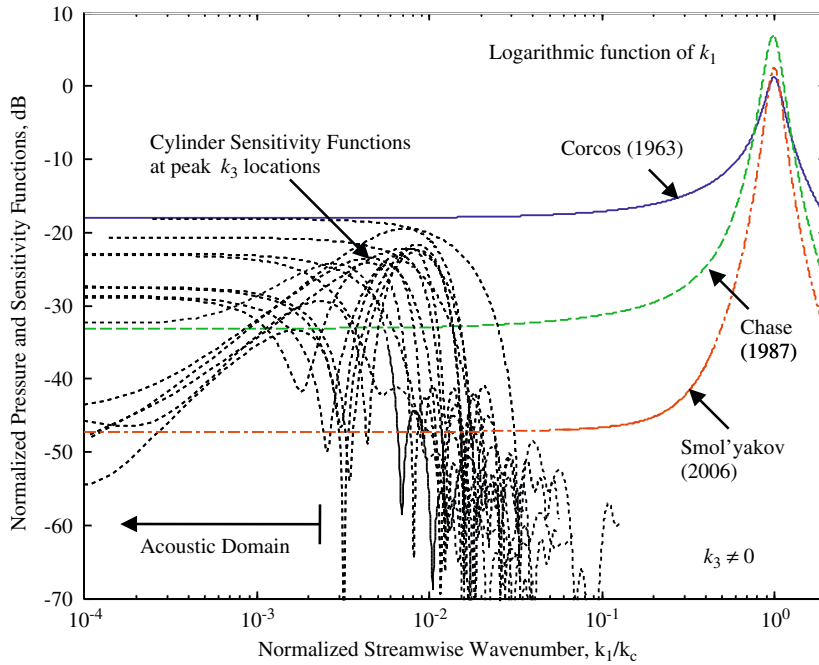
Fig. 9. Relationship between the streamwise low-wavenumber spectrum and measured sensitivity functions for identified cylindrical shell modes-logarithmic function of k_1.
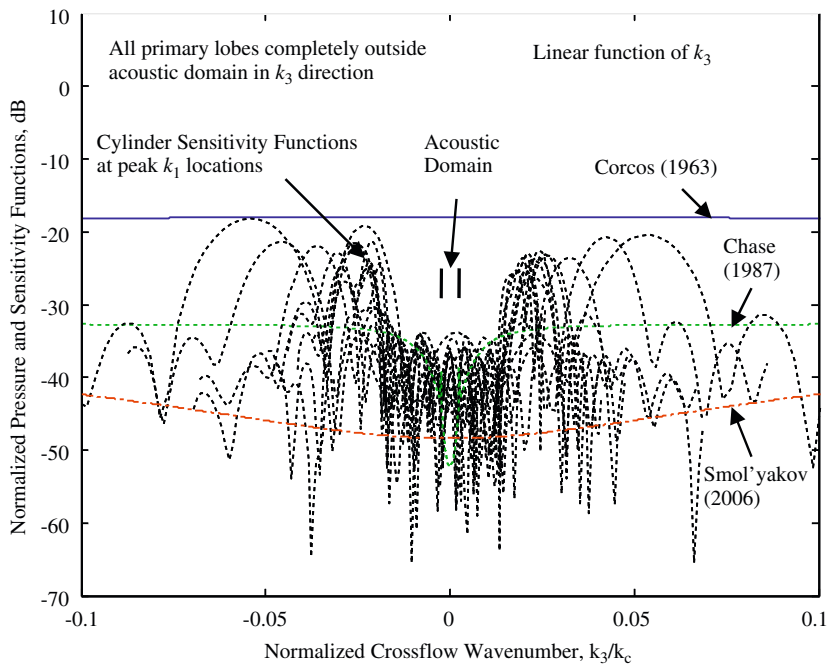

Fig. 10. Relationship between the cross-flow low-wavenumber spectrum and measured sensitivity functions for identified cylindrical shell modes-linear function of k_1.

modal test data. None of the $n=0$ modes can be identified. Because the 1,1 mode is highly damped, it is not apparent in Figs. 7 and 8. An analytical model [34] suggests the $n=0$ modes have a very low response due to the effect of mass loading from internal water on these mode shapes. Also, because the damping for these low-order modes is likely relatively high (as is indicated by the 1,1 mode), they are likely difficult to excite and identify.

Figs. 9 and 10 show the measured sensitivity functions for identified cylindrical shell modes and the location of the primary lobes relative to the TBL wavenumber spectrum. The primary lobes are centered below $k_1/k_c < 0.01$ in the k_1 direction and all fall completely outside the acoustic domain in the k_3 direction. The modal masses for identified modes determined using Eq. (5) are listed in Table 1 and range from 1.5 kg for the higher-order modes to 3.8 kg for the lowest-order mode.

4.3. Measured TBL vibration levels compared with historical TBL model estimates

Using the modal parameters and measured mode shapes for the modes listed in Table 1 and assuming a constant low-wavenumber TBL pressure level at and around the modal wavenumbers, the modal force is computed from Eq. (7) for each mode. Cylinder vibration spectra are estimated from Eq. (6) for the accelerometer locations measured with flow shown in Fig. 5 (three rings of 12 locations each). The constant low-wavenumber pressure spectrum levels required to match each estimated resonance peak with the measured flow data are reported in Table 1 and plotted versus wavenumber in Fig. 11.

Fig. 11 shows the constant low-wavenumber pressure spectrum levels derived from these experiments compared to historical data along with representative curves from the three TBL wavenumber models described previously. The plotted values represent two-sided functions of k_1, k_3, and ω. The Chase point frequency spectrum (Eq. (4) with high frequency exponential decay factor included) is used to convert the historical data from the form in which it was originally reported (discussed below) to the form of Fig. 11. Although the primary lobes for these modes extend over a range of wavenumbers, each pressure value is represented at its maximum k_1 and k_3 value in Fig. 11.

The low-wavenumber pressure values derived from these experiments fall midway between the Smol'yakov and Chase TBL models and roughly 23 dB lower than the Corcos model. The levels extracted from these data are slightly below the lower bound of the measurements by Martin and Leehey [4] and Farabee and Geib [21]. Farabee and Geib suggest the data measured at the lowest speed during their experiment (represented by the four lowest values in level and wavenumber) are the least likely to be contaminated from convective and acoustic sources.

Chase [10] suggests several model forms showing a power-law dependence to fit available low-wavenumber data. The simplest of these forms is both scale independent and wavenumber white

$$P(k_1, k_3, \omega)_{\text{low-wavenumber}} = C_0 \rho^2 u_t^6 \omega^{-3}. \tag{10}$$

Chase [35] refers to a fit of the Martin and Leehey [4] data with this form where $C_0 = 10^{-0.9}$ as the "Martin–Leehey" level which represents a single-sided function of k_1 in Eq. (10).

Fig. 12 shows the same data as Fig. 11 replotted in the form both Martin and Leehey [4] and Farabee and Geib [21] originally reported their results. The pressure levels in this plot are single-sided in k_1 and are non-dimensionalized by dynamic pressure rather than the point frequency spectrum used in Fig. 11. A constant low-wavenumber value
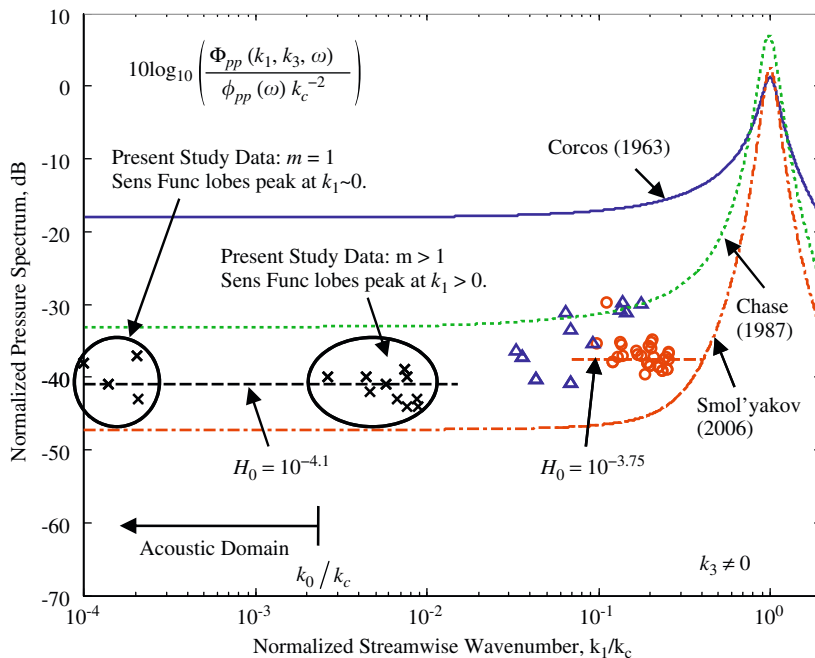

Fig. 11. Measured low-wavenumber pressure spectrum levels as a function of non-dimensional wavenumber: × present study, ○ Martin and Leehey data [1]; △ Farabee and Geib data [18].
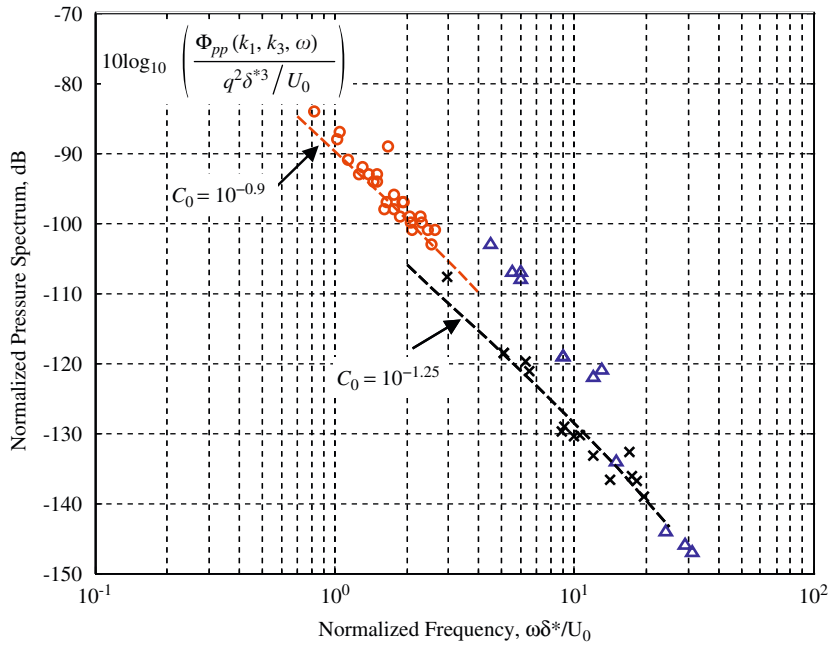
Fig. 12. Measured low-wavenumber pressure spectrum levels as a function of non-dimensional frequency: × present study, ○ Martin and Leehey data [1]; △ Farabee and Geib data [18].

(depicted in Fig. 11) corresponding to a point frequency spectrum which falls entirely within the universal range (where $\phi(\omega) \approx \rho^2 u_t^4 \omega^{-1}$) translates to a line in Fig. 12 which has a slope of $(\omega\delta^*/U_0)^{-3}$. This slope is consistent with the Chase model of Eq. (10). In the non-dimensional form of Fig. 12, no wavenumber dependence can be determined. It is best to view this plot as representing all low-wavenumber data without regard to where in the low-wavenumber spectrum it occurs.

Martin and Leehey report a least squares fit to their data showing a slope of $(\omega\delta^*/U_0)^{-3.34}$. Farabee and Geib suggest their highest reduced frequency data (least likely to be contaminated) shows a $(\omega\delta^*/U_0)^{-4}$ dependence. This difference in slope is likely due to the difference in slope of the respective point frequency spectra. The Martin and Leehey data fall almost entirely within the universal range where $\phi(\omega) \sim \omega^{-1}$. The Farabee and Geib data extend into the viscous subrange region (exponential roll-off) where the frequency dependence of $\phi(\omega)$ is steeper than ω^{-1}.

Since the simple Chase model of Eq. (10) is scale independent (universal range of the point frequency spectrum), it does not adequately model the low-wavenumber pressure levels at high reduced frequency. The exponential decay factor, $e^{-2.2(\omega v/u_\tau)}$, can be appended to Eq. (10), as was done for Eq. (4), to better fit the data shown in Fig. 12. The dashed line in Fig. 12 which runs through the Martin and Leehey data is plotted using

$$P(k_1,k_3,\omega)_{\text{low-wavenumber}} = C_0 \rho^2 u_t^6 \omega^{-3} e^{-2.2(\omega v/u_\tau)}, \tag{11}$$

where $C_0 = 10^{-0.9}$.

The current data set is also plotted in Fig. 12. The dashed line running through this data comes from plotting Eq. (11) where $C_0 = 10^{-1.25}$ which corresponds to the constant low-wavenumber value for this data identified from Fig. 11. The value of C_0 determined for the current data is 3.5 dB below the "Martin–Leehey" level.

The non-dimensionalization scheme of Fig. 11 suggests a slightly different form for the low-wavenumber pressure levels, where

$$P(k_1,k_3,\omega)_{\text{low-wavenumber}} \approx H_0 \phi(\omega) k_c^{-2} \tag{12}$$

Eq. (12) represents two-sided functions of k_1, k_3, and ω. For frequencies within or above the universal range of $\phi(\omega)$ this leads to a wavenumber white form of pressure

$$P(k_1,k_3,\omega)_{\text{low-wavenumber}} = H_0 \rho^2 u_t^4 U_c^2 \omega^{-3} e^{-2.2(\omega v/u_\tau)}. \tag{13}$$

The current data shown in Fig. 11 yields the constant, $H_0 = 10^{-4.1}$. As in Fig. 12, this level represents a 3.5 dB reduction from the "Martin and Leehey" level, however Fig. 11 also suggests the Martin and Leehey data measured at higher reduced wavenumbers may be slightly elevated by the tail of the convective ridge.

Eq. (13) reveals a dependence on convection velocity not present in the modified simple Chase model of Eq. (11). The point frequency spectrum contains a friction velocity to the fourth dependence and the associated wavenumber spectrum contains convection velocity squared dependence. The current data suggest the low-wavenumber domain of TBL pressures can be reasonably represented using the wavenumber white forms of Eqs. (11)–(13).

5. Summary, conclusions, and recommendations

In this experimental investigation, a thin cylindrical shell is used to inversely determine the low-wavenumber TBL surface pressure levels required to generate the cylinder's measured response to fully developed pipe flow at 6.1 m/s in water. Modal parameters of the experimental cylinder are used to determine these TBL surface pressure levels. They are determined from vibration measurements of the flow excited cylinder tests and an experimental modal analysis of the thin-walled cylindrical shell. The measured cylinder vibration due to flow excitation shows much of the same spectral content as the experimental modal analysis data.

Assuming a constant low-wavenumber TBL wall pressure level at and around the modal wavenumber, cylinder vibration spectra for various cylinder modes are estimated from Eq. (6). The constant low-wavenumber pressure spectrum level which best represents the measured flow data has a non-dimensional value of -41 dB (see Fig. 11). This leads to the wavenumber white forms for the TBL surface pressure spectrum at low-wavenumber suggested in Eq. (12) and (13).

The low-wavenumber pressure level derived from these experiments falls midway between the Smol'yakov [15] and Chase [13] TBL wavevector–frequency models and is roughly 23 dB below the Corcos [5] model. The level extracted from the current data is a few dB below the lower bound of measurements by Farabee and Geib [21] and Martin and Leehey [4].

An important aspect of the structural response to TBL excitation not addressed in this study is the role of viscosity or rotational effects that lead to the generation of increased fluctuating wall shear stress at low wavenumbers. Chase [35] suggested that viscosity induced shear stress, which has been neglected in most prior analyses, may be important in certain applications of TBL excitation. This is especially true for cylindrical and other shell structures where directional coupling exists for most modes. The procedures and data developed in this work can be extended to address inverse measurements of wall shear stress in the streamwise and cross-flow directions using primarily axial and circumferential cylindrical shell modes.

Another important aspect of the structural response to TBL excitation not addressed in this study and one which has received relatively little attention is the effect of surface roughness on low-wavenumber TBL wall pressures [36,37]. While this study focuses on establishing the smooth wall levels of TBL surface pressure, the current measurement facility and approach could be readily extended to provide a systematic evaluation of TBL wall pressure and surface roughness.

References

[1] P. Leehey, Structural excitation by a turbulent boundary layer: an overview, *Journal of Vibration, Acoustics, Stress, and Reliability in Design* 110 (April) (1988) 220–225.
[2] M.K. Bull, Wall-pressure fluctuations beneath turbulent boundary layers: some reflection on forty years of research, *Journal of Sound and Vibration* 190 (3) (1996) 299–315.
[3] W.R. Graham, A comparison of models for the wavenumber–frequency spectrum of turbulent boundary layer pressures, *Journal of Sound and Vibration* 206 (4) (1997) 542–565.
[4] N.C. Martin, P. Leehey, Low wavenumber wall pressure measurements using a rectangular membrane as a spatial filter, *Journal of Sound and Vibration* 52 (1) (1977) 95–120.
[5] G.M. Corcos, Resolution of pressure in turbulence, *Journal of the Acoustical Society of America* 35 (2) (1963) 192–198.
[6] W.W. Willmarth, C.E. Wooldridge, Measurements of the Fluctuating pressure at the wall beneath a thick turbulent boundary layer, *Journal of Fluid Mechanics* 14 (1962) 187–210.
[7] H.P. Bakewell, G.F. Carey, J.J. Libuka, H.H. Schloemer, W.A. Von Winkle, Wall Pressure Correlations in Turbulent Pipe Flow, *US Navy Underwater Sound Laboratory Report*, No. 559 (1962).
[8] J.E. Ffowcs Williams, Boundary-layer pressures and the Corcos model: a development to incorporate low wavenumber constraints, *Journal of Fluid Mechanics* 125 (1982) 9–12.
[9] S.H. Ko, H.H. Schloemer, Calculations of turbulent boundary layer pressure fluctuations transmitted into a viscoelastic layer, *Journal of the Acoustical Society of America* 85 (4) (1989) 1469–1477.
[10] D.M. Chase, Modeling the wavevector–frequency spectrum interaction, *Journal of Sound and Vibration* 70 (1980) 29–67.
[11] P.D. Lysak, Modeling the wall pressure spectrum in turbulent pipe flows, *Journal of Fluids Engineering* 128 (2006) 216–222.
[12] R.H. Kraichnan, Pressure fluctuations in turbulent flow over a flat plate, *Journal of the Acoustical Society of America* 28 (3) (1956) 378–390.
[13] D.M. Chase, The character of the turbulent wall pressure spectrum at subconvective wavenumbers and a suggested comprehensive model, *Journal of Sound and Vibration* 112 (1987) 125–147.
[14] D.M. Chase, Fluctuating wall-shear stress and pressure at low streamwise wavenumbers in turbulent boundary-layer flow at low mach numbers, *Journal of Fluids and Structures* 6 (1992) 395–413.
[15] A.V. Smol'yakav, A new model for the cross spectrum and wavenumber–frequency spectrum of turbulent pressure fluctuations in a boundary layer, *Acoustical Physics* 52 (3) (2006) 331–337.
[16] A.V. Smol'yakav, V.M. Tkachenko, Model of a field of pseudosonic turbulent wall pressures and experimental data, *Soviet Physical Acoustics* 37 (1991) 627–631.
[17] A.V. Smol'yakav, Calculation of the spectra of pseudosound wall-pressure fluctuations in turbulent boundary layers, *Acoustical Physics* 46 (3) (2000) 342–347.
[18] B.M. Efimstov, Characteristics of the field of turbulent wall pressure fluctuations at large Reynolds numbers, *Soviet Physics—Acoustics* 28 (4) (1982) 289–292.

[19] G. Maidanik, Flush-mounted pressure transducer systems as spatial and spectral filters, *Journal of the Acoustical Society of America* 42 (5) (1967) 1017–1024.
[20] W.K. Blake, D.M. Chase, Wavenumber–frequency of turbulent-boundary-layer pressure measured by microphone arrays, *Journal of the Acoustical Society of America* 49 (3) (1971) 1017–1024.
[21] T.M. Farabee, F.E. Geib, Measurement of boundary layer pressure fields with an array of pressure transducers in a subsonic flow, *ICIASF '75 Record*, 1975, pp. 311–319.
[22] E. Manoha, The wavenumber–frequency spectrum of the wall pressure fluctuations beneath a turbulent boundary layer, *Second AIAA/CEAS Aeroacoustics Conference*, May 6–8, 1996, State College, PA.
[23] B.M. Abraham, W.L. Keith, Direct measurements of turbulent boundary layer wall pressure wavenumber–frequency spectra, *Journal of Fluids Engineering* 120 (1998) 29–39.
[24] D.J. Ewins, *Modal Testing: Theory, Practice, and Applications*, 2nd ed, Research Studies Press, Hertfordshire, England, 2001.
[25] Y.F. Hwang, G. Maidanik, A wavenumber analysis of the coupling of a structural mode and flow turbulence, *Journal of Sound and Vibration* 142 (1) (1990) 135–152.
[26] M.C. Marboe, R.M. Weyer, M.L. Jonson, D.E. Thompson, Hydroacoustic research capabilities in the large water tunnel at ARL Penn State, *ASME NCA Division Publication* 15 (1993) 125–135.
[27] E.M. Laws, Flow conditioning—a new development, *Flow Measurement Instrumentation* 1 (3) (1990) 165–170.
[28] G.C. Lauchle, M.A. Daniels, Wall-pressure fluctuations in turbulent pipe flow, *Physics of Fluids* 30 (10) (1987) 3019–3024.
[29] J.S. Bendat, A.G. Persol, *Random Data—Analysis and Measurement Procedures*, John Wiley & Sons, Inc., New York, NY, 1986.
[30] N. Catbas, D.L. Brown, A.E. Aktan, Parameter estimation for multiple-input multiple-output modal analysis of large structures, *Journal of Engineering Mechanics* 130 (8) (2004) 921–930.
[31] S.H. Ko, Performance of various shapes of hydrophones in the reduction of turbulent flow noise, *Journal of the Acoustical Society of America* 93 (3) (1993) 1293–1299.
[32] M.K. Bull, Wall pressure fluctuations associated with subsonic turbulent boundary layer flow, *Journal of Fluid Mechanics* 28 (4) (1967) 719–754.
[33] W.L. Keith, D.A. Hurdis, B.M. Abraham, Comparison of turbulent boundary layer wall-pressure spectra, *Journal of Fluids Engineering* 114 (1992) 338–347.
[34] E.A. Skelton, J.H. James, *Theoretical Acoustics of Underwater Structures*, Imperial College Press, 1997 (pp. 373–381).
[35] D.M. Chase, A semi-empirical model for the wavevector–frequency spectrum of turbulent wall-shear stress, *Journal of Fluids and Structures* 7 (1993) 639–659.
[36] W.K. Blake, Turbulent boundary-layer wall-pressure fluctuations on smooth and rough walls, *Journal of Fluid Mechanics* 44 (4) (1970) 637–660.
[37] M.S. Howe, Surface pressure and sound produced by turbulent flow over smooth and rough walls, *Journal of Acoustical Society of America* 90 (2) (1991) 1041–1047.